Research Square

Preprints are preliminary reports that have not undergone peer review.
They should not be considered conclusive, used to inform clinical practice,
or referenced by the media as validated information.

Proton-Coupled Charge Transfer Induces a Magnetic Phase Transition in Layered Metal-Organic Frameworks

Hitoshi Miyasaka

hitoshi.miyasaka.e7@tohoku.ac.jp

Tohoku University https://orcid.org/0000-0001-9897-0782

Ke Ji

Tohoku University

Chisa Itoh

Tohoku University

Ryota Nasu

The University of Osaka

Kaito Taka

The University of Osaka

Ren Inoue

The University of Osaka

Wataru Kosaka

Tohoku University

Haruka Yoshino

Tohoku University

Yasutaka Kitagawa

The University of Osaka

Article

Keywords:

Posted Date: July 29th, 2026

DOI: https://doi.org/10.21203/rs.3.rs-10338641/v1

License: This work is licensed under a Creative Commons Attribution 4.0 International License.
Read Full License

Additional Declarations: There is **NO** Competing Interest.

Proton-Coupled Charge Transfer Induces a Magnetic Phase Transition in Layered Metal-Organic Frameworks

Ke Ji,[a,b] Chisa Itoh,[a,b] Ryota Nasu,[c] Kaito Taka,[c] Ren Inoue,[c] Wataru Kosaka,[a,b] Haruka Yoshino,[a,b] Yasutaka Kitagawa,[c] and Hitoshi Miyasaka*[a,b]

[a] Institute for Materials Research, Tohoku University, 2-1-1 Katahira, Aoba-ku, Sendai 980-8577, Japan

[b] Department of Chemistry, Graduate School of Science, Tohoku University, 6-3 Aramaki-Aza-Aoba, Aoba-ku, Sendai 980-8578, Japan

[c] Department of Materials Engineering Science, Graduate School of Engineering Science, The University of Osaka, 1-3 Machikaneyama, Toyonaka, Osaka 560-8531, Japan

Corresponding author*

Prof. Dr. Hitoshi Miyasaka

Institute for Materials Research

Tohoku University

2-1-1 Katahira, Aoba-ku, Sendai 980-8577, Japan

E-mail: hitoshi.miyasaka.e7@tohoku.ac.jp

Tel: +81-22-215-2030

FAX: +81-22-215-2031

Abstract

Proton-coupled charge transfer (PCCT), a fundamental principle underlying biological electron transport, has rarely been realized in crystalline materials, where the charge, proton, and spin degrees of freedom can be cooperatively controlled. Herein, we report a redox-active layered donor (D)–acceptor (A) metal-organic framework (D_2A-MOF), in which modulation of the intramolecular hydrogen bonds (HBs) acts as a decisive trigger for intralattice charge transfer and a concomitant magnetic phase transformation. The framework is constructed from an *o*-hydroxybenzoate-bridged paddlewheel-type diruthenium(II,II) complex as the D unit and bis[1,2,5]dithiazolotetracyanoquinodimethane (BTDA-TCNQ) as the A unit. Systematic solvent desorption selectively disrupts the intramolecular HB between the *o*-hydroxy group and the carboxylate oxygen, effectively converting the D unit into a D* state at a higher potential. This HB-mediated electronic reorganization induces a one-electron transfer from [Ru_2] to BTDA-TCNQ, generating a [–$\{Ru_2\}^{+}$–$(BTDA\text{-}TCNQ)^{\bullet-}$–$\{Ru_2\}^{0}$–] state that converts the material from a paramagnet to an antiferromagnet with a Néel temperature of 58 K. Density functional theory (DFT) calculations corroborate the decisive role of HB mode switching in tuning the highest occupied molecular orbital (HOMO) level of the donor and enabling charge transfer. This study establishes modulation of intramolecular HBs as a powerful design principle for PCCT in MOFs and demonstrates a chemically triggered magnetic phase transition driven by guest-controlled proton dynamics.

Introduction

Proton-coupled electron transfer (PCET), in which electron transfer is intimately coupled to protonation/deprotonation processes or to the modulation of hydrogen bond (HB) configurations, constitutes one of the most fundamental mechanisms governing biological electron-transport and energy-conversion systems.[1,2,3,4,5] In natural systems, subtle proton displacements or local HB rearrangements can drastically alter the redox potentials of molecular subunits,[6] thereby regulating long-range charge migration, directional electron flow, and cooperative phase evolution.[4,7,8] Translating such proton-coupled electronic regulation into synthetic crystalline materials has therefore emerged as an important challenge at the interface of coordination chemistry, condensed-matter science, and materials chemistry.[9,10,11,12] In particular, materials capable of coupling proton dynamics with collective electronic state transformations are expected to provide new opportunities for chemically responsive switching materials, adaptive magnetic systems, and stimuli-responsive electronic phases.[9,10,11,12]

Metal-organic frameworks (MOFs) provide an especially attractive platform for realizing such concepts because their frameworks intrinsically combine lattice functionality with accessible internal space.[13,14] Unlike conventional rigid inorganic solids, MOFs can dynamically respond to adsorption/desorption and mass transport of guest molecules through cooperative structural and electronic modulations.[14,15,16,17,18] The chemical environment within the pores therefore may influence not only local coordination geometries but also bulk electronic states, spin configurations, and intermolecular interactions.[17,19,20,21,22,23,24] This unique combination of "combination of a functional lattice and accessible pore space" has established MOFs as important materials for guest-responsive phenomena.[14,15,16,17,18,20,21] Nevertheless, despite the extensive development of MOFs and related coordination polymers (CPs), there are relatively few examples in which guest transport directly induces charge transfer (CT) within the host lattice.[24,25,26,27,28,29] Moreover, the explicit realization of proton-coupled charge transfer (PCCT) in crystalline porous frameworks remains exceptionally rare.[30,31]

Among the various classes of redox-active MOFs, donor/acceptor frameworks (D/A-MOFs) composed of electron-donating (D) and electron-accepting (A) molecular subunits provide a particularly promising strategy for realizing cooperative electronic-state switching.[32,33] We have previously developed a family of D/A-MOFs composed of paddlewheel diruthenium(II,II) complexes ($[Ru_2^{II,II}]$) as the D unit and 7,7,8,8-tetracyano-*p*-quinodimethane (TCNQ) derivatives ($TCNQR_x$) as the A unit.[32,33] These systems predominantly form layered D_2A-MOF architectures containing two D units and one A unit (Fig. 1a).[34] Depending on the degree of CT between the D and A units, these materials exhibited markedly different magnetic and electronic properties.[34,35,36,37] The one-electron-transferred state (1e-I; $D^{0.5+}{}_2A^-$ or $D^+D^0A^-$) generates low-dimensional magnetic lattices composed of exchange-coupled radical spins of $TCNQR_x^{\bullet-}$, whereas the neutral state (N; $D^0{}_2A^0$) and two-electron-transferred state (2e-I; $D^+{}_2A^{2-}$) are essentially paramagnetic (PM). Importantly, these layered D_2A-MOFs also possess moderate porosity, allowing the adsorption of volatile guests and common gases such as O_2, N_2, and CO_2, which can substantially perturb the charge distribution, spin alignment, and magnetic ordering.[24,25,26,27,28,29,38,39]

<<Insert Fig. 1 here>>

In this context, guest-responsive control of electronic states in D/A-MOFs has recently attracted increasing attention because cooperative interactions among the lattice, charge, spin, and guest molecules can produce emergent magnetic and electronic phenomena that are inaccessible in conventional dense inorganic solids.[33] However, in most reported systems, guest-induced CT transitions are accompanied by substantial lattice deformation, layer corrugation, and framework breathing.[39] Consequently, it is difficult to experimentally isolate the intrinsic role of proton displacement or HB modulation in controlling CT processes of the framework. A system in which local proton rearrangement itself acts as the primary trigger for CT would provide an important conceptual advancement toward proton-coupled electronic-state engineering in MOF materials.

In the PCCT process, the modulation of protonation/deprotonation states or HB configurations generates a specific state of the donor (D*) or acceptor (A*) species with enhanced electron-donating or electron-accepting abilities, respectively. Such modulation can induce CT from D* to A or from D to A* (Fig. 1b). Although this mechanism has been implied in several molecular systems, no porous framework has explicitly demonstrated the systematic control of framework CT through the modulation of intramolecular HB modes.

To address this challenge, here we focused on *o*-hydroxybenzoate-bridged paddlewheel diruthenium(II,II) complexes, $[Ru_2(R\text{-}2\text{-}OHArCO_2)_4]$, whose donor ability is highly sensitive to intramolecular HB configurations.[40,41,42] Unexpectedly, the *o*-OH substituent was found to lower the highest occupied molecular orbital (HOMO) energy level because the intramolecular O–H···O HB exerts a strong electron-withdrawing effect (HB-normal mode; Fig. 1b), contrary to the conventional expectation that an OH group behaves primarily as an electron donor. If the proton rotates away from the carboxylate oxygen atom and the intramolecular HB is disrupted (HB-preventing mode; Fig. 1b), the HOMO energy level rises substantially, effectively generating a stronger donor species D*. Density functional theory (DFT) calculations suggested that disruption of the intramolecular HB can increase the donor HOMO energy level by approximately 0.5 eV per *trans* pair, which is sufficiently large to alter the donor–acceptor energy balance in a D/A-MOF framework.[40,41,42]

Based on this concept, we designed a layered D_2A-MOF comprising $[Ru_2(4\text{-}F\text{-}2\text{-}OHArCO_2)_4]$ ($4\text{-}F\text{-}2\text{-}OHArCO_2^-$ = 4-fluoro-2-hydroxybenzoate) donors[42] and bis[1,2,5]dithiazolotetracyanoquinodimethane (BTDA-TCNQ) acceptors[43] (Fig. 1a). The resulting compound, $[\{Ru_2(4\text{-}F\text{-}2\text{-}OHArCO_2)_4\}_2(BTDA\text{-}TCNQ)]\cdot 3(anisole)$ (**1-3Ani**), initially adopts a neutral electronic state with intact intramolecular HBs and therefore exhibits paramagnetic (PM) behavior. Stepwise desolvation first yields $[\{Ru_2(4\text{-}F\text{-}2\text{-}OHArCO_2)_4\}_2(BTDA\text{-}TCNQ)]\cdot 2(anisole)$ (**1-2Ani**), which retains the neutral state (Fig. 1c), and subsequently produces the solvent-free phase $[\{Ru_2(4\text{-}F\text{-}2\text{-}OHArCO_2)_4\}_2(BTDA\text{-}TCNQ)]$ (**1**), in which disruption of intramolecular HBs in one donor unit induces intralattice CT to BTDA-TCNQ (Fig. 1d). The resulting 1e-I ionic phase forms

ferrimagnetic layers that exhibit antiferromagnetic (AFM) interlayer coupling with a Néel temperature (T_N) of 58 K.

Importantly, the layered framework topology is largely preserved during this transformation, enabling direct identification of HB modulation as the principal trigger for CT. Local proton rearrangement elevates the HOMO level of D to create D* and cooperatively stabilizes the ionic state through the accompanying local structural relaxation. Therefore, this study provides the first explicit realization of framework CT governed by the modulation of intramolecular HB modes and establishes a new mechanism for PCCT in MOF materials. More broadly, these findings demonstrate how proton dynamics and HB engineering can be integrated into redox-active MOFs to achieve cooperative control of charge, spin, and magnetic phase behaviors.

Results

Design concept of electron-proton modular systems

To evaluate the influence of the HB modes on the donor ability of [Ru_2(4-F-2-OHArCO_2)$_4$], DFT calculations were performed using models derived from the crystal structure of [Ru_2(4-F-2-OHArCO_2)$_4$(THF)$_2$] (Fig. 1e).[42] The proton positions in the *o*-OH groups were systematically rotated around the Ar–O bond axis (C_{Ar}(2)–O_{OH} bond), where the rotation angle ($\Delta\theta$) was defined as the dihedral angle between the plane formed by C_{Ar}(1)–C_{Ar}(2)–O_{OH} and the plane formed by C_{Ar}(2)–O_{OH}–H_{OH} in the Ar–O–H group (Fig. 1f). The condition $\Delta\theta$ = 0° was defined as the original intramolecular HB geometry (Bz1: –2.60°, Bz2: 2.61°), whereas the fully HB-disrupted structure corresponds to $\Delta\theta$ = 180°. Due to the presence of an inversion center at the midpoint of the Ru–Ru bond in the [Ru_2(4-F-2-OHArCO_2)$_4$(THF)$_2$] complex, the hydrogen atoms in the set of *trans*-positioned 4-F-2-OHArCO_2^- ligands (Bz1 and Bz2, respectively) were identical (Fig. 1e).

The HOMO energy level of the original HB-normal structure was calculated to be −4.9922 eV. The rotation of one set of *trans*-positioned *o*-OH protons raised the HOMO level to approximately −4.50 eV in $\Delta\theta$ = 180°, whereas the simultaneous rotation of both sets increased it to −4.00334 eV

(Table S1, Fig. 1g). Thus, the disruption of one intramolecular HB pair increased the HOMO level by approximately 0.5 eV, while the disruption of two pairs increased it by approximately 1 eV.

For D_2A-MOFs constructed from $[Ru_2(4\text{-F-2-OHArCO}_2)_4]$ and BTDA-TCNQ, the CT tendency can be approximately estimated from the energy difference between the donor HOMO ($HOMO_D$) and acceptor LUMO ($LUMO_A$), i.e., $\Delta E_{HL}(DA) = E_L(A) - E_H(D)$. The LUMO energy of BTDA-TCNQ was calculated to be −4.7353 eV. Therefore, the HB-normal donor state possesses a lower $HOMO_D$ level than the $LUMO_A$ level and therefore favors the neutral state ($\Delta E_{HL}(DA)$ = 0.2569 eV). In contrast, the HB-disrupted D* state possesses a sufficiently elevated $HOMO_D$* level to satisfy $\Delta E_{HL}(DA) < 0$, thereby favoring the CT state: $\Delta E_{HL}(DA)$ = –0.2353 eV for the model where one pair of *trans*-positioned *o*-OH protons are disrupted. These results strongly suggest that the modulation of intramolecular HBs can control CT in the layered framework.

Synthesis and spectroscopic characterization

Compound **1-3Ani** was synthesized as dark-brown block crystals by the slow diffusion of a benzene solution of BTDA-TCNQ into an anisole solution of $[Ru_2^{II,II}(4\text{-F-2-OHArCO}_2)_4(THF)_2]$. Thermogravimetric (TG) measurements under dry N_2 showed stepwise weight losses corresponding to one anisole molecule near 373 K and two additional anisole molecules near 471 K, followed by decomposition at approximately 497 K (Fig. S1a). These results indicate the presence of two crystallographically distinct anisole environments (see the Crystallography section).

The Fourier-transform infrared (FT-IR) spectrum of **1-3Ani** displayed $\nu_{C\equiv N}$ bands at 2239, 2223, 2196, and 2170 cm^{-1}, characteristic of neutral BTDA-TCNQ (Fig. S2).[44] The Raman spectrum exhibited $\nu_{C=C}$ and $\nu_{C\equiv N}$ bands at 1540 and 2228 cm^{-1}, respectively, also consistent with the neutral acceptor state [the original neutral BTDA-TCNQ component exhibited characteristic Raman bands at 1565 cm^{-1} for $\nu_{C=C}$ and at 2230 and 2220 cm^{-1} for $\nu_{C\equiv N}$, respectively] (Fig. S3).[45]

According to the TG profile, the selective removal of one anisole molecule produced a stable, partially desolvated species, **1-2Ani** (Fig. S1a). TG analysis of **1-2Ani** showed gradual loss of the

remaining two anisole molecules up to approximately 473 K (Fig. S1b). The FT-IR and Raman spectra remained essentially unchanged relative to those of **1-3Ani**, indicating retention of the neutral electronic state [$\nu_{C\equiv N}$ bands at 2240, 2224, 2197, and 2170 cm^{-1} in the IR spectra; $\nu_{C=C}$ and $\nu_{C\equiv N}$ bands at 1542 and 2232 cm^{-1}, respectively, in the Raman spectra of **1-2Ani**] (Fig. S3).

Further heating of **1-2Ani** to 393 K removed the remaining anisole molecules and produced the solvent-free compound **1** without loss of crystallinity. The FT-IR spectrum showed clear shifts of the $\nu_{C\equiv N}$ bands to 2195 and 2171 cm^{-1}, consistent with the formation of BTDA-$TCNQ^{\bullet-}$ (Fig. S2).[44,45,46] The Raman spectrum exhibited $\nu_{C=C}$ and $\nu_{C\equiv N}$ bands at 1513 and 2221 cm^{-1}, respectively, also characteristic of the radical-anion state [Li^{+}BTDA-$TCNQ^{\bullet-}$ exhibits distinctive Raman bands at 1530 cm^{-1} for $\nu_{C=C}$ and 2217 cm^{-1} for $\nu_{C\equiv N}$, as shown in Fig. S3].[45] These spectroscopic changes unequivocally demonstrate that desolvation from **1-2Ani** to **1** induces intralattice CT from the donor framework to BTDA-TCNQ.

Powder X-ray diffraction (PXRD; Fig. S4), *in situ* PXRD (Fig. S5), and elemental analysis (see the Methods section) confirmed the phase purity of **1-3Ani**, **1-2Ani**, and **1**. Re-exposure of **1** to anisole regenerated the original phase, denoted as **1-reAni** (Fig. S4), accompanied by restoration of the spectral features of neutral BTDA-TCNQ (Fig. S2 and S3).

Crystal structures and electronic-state evolution

The structural features of the present compounds are particularly important because they indicate that the present PCCT mechanism is fundamentally distinct from conventional guest-induced CT transitions that are primarily driven by lattice-energy stabilization.[39] Instead, modulation of the donor potential through proton displacement and HB rearrangement plays a dominant role.

Compound **1-3Ani** crystallizes in the triclinic $P\bar{1}$ space group with inversion centers located at two independent [Ru_2] units, [$Ru(1)_2$] and [$Ru(2)_2$], and at the BTDA-TCNQ moiety ($Z = 1$) (Table S2, Fig. 2a). The structure consists of fishnet-like two-dimensional layers lying on the (110) plane and stacked along the *a*-axis (Fig. 2b and 2c). Three anisole molecules occupy the interlayer voids,

which have a total volume of 530 Å^3 (25.2% of the crystal volume). Two anisole molecules (Ani-1) form π-stacking interactions with BTDA-TCNQ (Fig. S6a), whereas the third anisole molecule (Ani-2) interacts with the benzoate ligands (Bz3) on the neighboring [Ru(2)$_2$] units (Fig. S6b).

<<Insert Fig. 2 here>>

Electronic states were evaluated based on the characteristic bond lengths. The average Ru−O$_{eq}$ distances of 2.0633(10) and 2.058(2) Å for [Ru(1)$_2$] and [Ru(2)$_2$], respectively, are consistent with the [Ru$_2^{II,II}$] state (Table S3), because the typical values are within the ranges of 2.06−2.07 for [Ru$_2^{II,II}$] and 2.02−2.03 Å for [Ru$_2^{II,III}$]$^+$.[47] The Kistenmacher relationship yielded a BTDA-TCNQ charge value of ρ = –0.65(5) (Table S4), indicating a neutral acceptor state.[48] Despite some overestimation of charge, BTDA-TCNQ^0 can still be considered to be in the neutral state, consistent with previously reported neutral BTDA-TCNQ compounds ($\rho \approx -0.6$).[45,46] These assignments are fully consistent with the spectroscopic data.

Compound **1-2Ani** also crystallizes in *P*−1 and retains the layered framework (Fig. 2d–2f). The removal of Ani-2 reduces the void volume to 391 Å^3 (19.2% of the total volume, including the space occupied by two Ani-1 molecules and the void left by Ani-2), but the structural changes remain minimal. The mean Ru−O$_{eq}$ distances of 2.0638(9) and 2.0582(9) Å for [Ru(1)$_2$] and [Ru(2)$_2$], respectively, and ρ = –0.50(4) for the BTDA-TCNQ moiety indicate that **1-2Ani** also remains in the neutral state (Tables S3 and S4).

Likewise, the solvent-free compound **1** preserves the layered framework (Fig. 2g–2i) but exhibits a dramatic change in its electronic state. The mean Ru−O$_{eq}$ distances are 2.0538(19) Å for [Ru(1)$_2$] and 2.0182(12) Å for [Ru(2)$_2$], corresponding to [Ru(1)$_2^{II,II}$] and [Ru(2)$_2^{II,III}$]$^+$, respectively (Table S3). The charge on BTDA-TCNQ becomes ρ = −1.40(7),[45, 49] indicating the formation of [−{Ru(1)$_2^{II,II}$}−{BTDA-TCNQ}$^{\bullet-}$−{Ru(2)$_2^{II,III}$}$^+$−], *i.e.*, a single-electron transfer from [Ru(2)$_2^{II,II}$] to BTDA-TCNQ during the desolvation process from **1-2Ani** to **1** (Table S4). Thus, the desolvation

sequence proceeds as N → N → 1e-I for **1-3Ani** → **1-2Ani** → **1**.

Although the unit cell volume decreased substantially during desolvation, the interlayer translational distances, corresponding to the *a*-axis, remained nearly constant at 10.3575(5), 10.3301(4), and 10.4147(3) Å for **1-3Ani**, **1-2Ani**, and **1**, respectively, compared with 10.4064(5) Å for **1-reAni**. This preservation of the layer spacing originates from the bending of the benzoate aryl groups into the vacated interlayer space (Table S5). Consequently, only minor structural changes accompany the electronic state transformation (Table S6).

Hydrogen-bond modulation as the trigger for charge transfer

The relationship between HB rearrangement and framework CT is the central mechanistic issue in the present study. Although desolvation naturally changes the local packing environment around the framework, as seen in the protrusion of the aryl ring of the benzoate ligands into the interlayer space produced during desolvation from **1-2Ani** to **1** (*vide infra*), the crystallographic data indicate that the overall lattice contraction is relatively small. In fact, the simulated PXRD data for **1-3Ani**, **1-2Ani**, and **1** show only slight peak shifts corresponding to the (011), (01–1), (110), (101), (10–1), and (002) indices at low 2θ angles during desolvation, without the appearance of new reflections (Fig. S7), confirming that the layered framework is largely preserved throughout the transformation. The slight change in the interlayer distance implies that the Madelung Coulombic stabilization gained from the structural transition might be minimal. Importantly, in previously reported guest-induced CT systems, neutral-to-ionic transitions were generally accompanied by pronounced structural rearrangements, such as transformations from flat to zigzag layer conformations.[24] In contrast, the present system exhibits only subtle structural modifications during the sequence **1-3Ani** → **1-2Ani** → **1**; the intralayer zigzag angle ψ remains nearly constant (Table S7). The absence of substantial layer deformation indicates that the CT process is not simply driven by structural compression or enhanced intermolecular overlap. Instead, the donor ability of the [Ru_2] unit itself changes *via* modulation of the intramolecular HB mode. Therefore, the present system enables the direct examination of whether

local proton displacement can sufficiently alter the donor potential (*i.e.*, generate D*) to trigger CT in the framework.

Of the two crystallographically independent donor units, only [Ru(2)$_2$] changes its oxidation state during the second desolvation step, from **1-2Ani** to **1**. In each [Ru$_2$] unit, the 4-F-2-OHArCO$_2^-$ ligands are designated as Bz1 and Bz2 in [Ru(1)$_2$] and Bz3 and Bz4 in [Ru(2)$_2$], as shown in Fig. 3a, c, e, and g. Importantly, only the Bz4 ligand associated with [Ru(2)$_2$] exhibits flip-flop disorder of the benzoate aryl moiety during the second desolvation step (Fig. 3f).

In the first desolvation step, the removal of Ani-2 mainly induces displacement of the Bz3 ligand of [Ru(2)$_2$] into the vacated space (Fig. S6). In the second desolvation step, the removal of two Ani-1 molecules generates larger voids that permit rotational motion of the Bz4 aryl group, with an occupancy of 0.45:0.55 for O(12A):O(12) (single-crystal X-ray diffraction (SCXRD) evaluation), as well as inclination disorder in Bz1 of [Ru(1)$_2$] (Fig. 3f). This motion disrupts the original intramolecular O–H···O HB and generates new intermolecular interactions, including O–H···F and O–H···π contacts with the distances of O(12A)$_H$···F (Bz1) = 2.37(2) Å and O(12)$_H$···C (Ar in Bz1) = 3.24(4) Å.[50] Note that most of the hydrogen positions identified by SCXRD and shown in Fig. 3 were determined using Fourier techniques based on free rotation, except for the hydroxy H atoms (H3A for Bz1 and H12A for Bz4) (see Methods). Therefore, the disorder of the *o*-OH group in Bz4 of [Ru(2)$_2$] is directly linked to solvent removal during the second desolvation process. Notably, the positional disorder of Bz1 originates from the crystal growth process and persists throughout the transformation, during which the intramolecular HB is preserved (Fig. 3a, c, e, and g). More importantly, this process is reversible. Upon re-adsorption of anisole, the original intramolecular HB mode is restored to **1-reAni**, and the framework returns to the neutral state (Fig. 3g, h and Fig. S2, S3).

<<Insert Fig. 3 here>>

Because the disruption of one pair of intramolecular HBs can raise the donor HOMO level by approximately 0.5 eV, the HOMO level of the [Ru(2)$_2$] donor unit exceeds the LUMO level of BTDA-TCNQ ($|\Delta E| \approx 0.23$ eV). Thus, the donor unit with disrupted HBs effectively acts as a stronger donor species, D*, triggering CT to the acceptor framework.

Magnetic properties of 1-3Ani and 1-2Ani

The magnetic properties of **1-3Ani** and **1-2Ani** are characteristic of neutral D_2A-MOFs containing magnetically isolated [$Ru_2^{II,II}$] units with $S = 1$ (Fig. 4a, b and Fig. S8c).[40,41,42,47] Field-cooled magnetization (FCM) measurements under a 1 kOe DC field yielded χT values of 1.84 and 2.05 cm^3 K mol^{-1} at 300 K for **1-3Ani** and **1-2Ani**, respectively, which are close to the expected value for two isolated $S = 1$ centers in each compound. Upon cooling, χT gradually decreases to 0.07 and 0.15 cm^3 K mol^{-1} at 1.8 K for **1-3Ani** and **1-2Ani**, respectively. The magnetic susceptibility data were analyzed using a Curie-type PM model incorporating zero-field splitting (D), temperature-independent paramagnetism (χ_{TIP}), and a small amount of [$Ru_2^{II,III}$]$^+$ impurity with $S = 3/2$ (ρ).[51,52] For **1-3Ani**, the best-fit parameters are $D/k_B = 373.2(16)$ K, $\chi_{TIP} = 77(19) \times 10^{-6}$ cm^3 mol^{-1}, and impurity ratio $\rho = 0.0684(11)$. For **1-2Ani**, the values are $D/k_B = 348(3)$ K, $\chi_{TIP} = 99(23) \times 10^{-6}$ cm^3 mol^{-1}, and $\rho = 0.0618(6)$. No magnetic hysteresis was observed at 1.8 K. These parameters are typical of isolated [$Ru_2^{II,II}$] complexes and clearly demonstrate that both compounds remain in the neutral PM state.[34,46,53,54]

<<Insert Fig. 4 here>>

Magnetic properties of solvent-free 1

The magnetic behavior of solvent-free **1** clearly demonstrates that the desolvation-induced CT transition is directly linked to the magnetic phase transformation (Fig. S8a). Because the neutral compounds **1-3Ani** and **1-2Ani** contain magnetically isolated [$Ru_2^{II,II}$] units separated by diamagnetic

BTDA-TCNQ molecules, they behave as conventional paramagnets. In contrast, the formation of BTDA-TCNQ$^{\bullet-}$ and $[Ru_2^{II,III}]^+$ in **1** introduces exchange-coupled spin carriers within the layered framework, showing an onset of magnetization at approximately 80 K under a 1 kOe DC field (Fig. 4c), providing direct evidence for the formation of the ionic 1e-I state. When a field smaller than 100 Oe was applied, a peak emerged near 60 K at weaker fields below approximately 50 Oe (inset of Fig. 4c and Fig. S8b). This indicates an AFM ground state for **1**. Despite this, the AC susceptibility measured under zero DC field exhibits a cusp at χ'' with weak frequency dependence; the onset of χ'' is 62 K (Fig. 4d). The presence of χ'' signifies residual magnetization resulting from spin canting or structural defects formed during desolvation, which interfere with the complete cancellation of AFM ordering between layers. Analysis of the frequency dependence indicates cluster-glass-like behavior (Fig. S9).[55,56] The χ' maximum at 58 K (1 Hz) defines the Néel temperature (T_N). Field-dependent magnetization measurements (M–H curves) reveal a metamagnetic spin-flipping behavior, and the critical fields (M_{ex}) extracted from dM/dH plots (Fig. 4e and S8d) allow the construction of an H–T phase diagram separating the AFM and PM phases (Fig. 4f). Once the material enters the PM phase with ferromagnetic (FM) spin configurations under sufficiently strong magnetic fields exceeding the critical field H_{ex} in the temperature range of $T < T_N$, the FM state remains even after removal of the external field, indicating field-induced ferromagnetism.

The AFM ground state is consistent with previously established magnetostructural correlations for layered $[Ru_2]_2TCNQR_x$ systems.[27,57] The practical interlayer translational distance l'_{trans} for **1** is 10.47 Å (Table S7), which is below the empirical threshold value of approximately 10.6 Å associated with the AFM interlayer coupling.[27]

Magnetic properties of 1-reAni

The re-adsorption of anisole into **1** restores the original neutral PM state. Compound **1-reAni** exhibits χT = 1.94 cm^3 K mol^{-1} at 300 K, which gradually decreases to 0.08 cm^3 K mol^{-1} at 1.8 K (Fig. S10). The magnetic susceptibility data were fitted using the same Curie-type model, giving D/k_B =

362.2(13) K, χ_{TIP} = 116.4(98) × 10^{-6} cm^3 mol^{-1}, and impurity ratio ρ = 0.0252(2).エラー！ ブックマークが定義されていません。,[52] Magnetic hysteresis was not observed. These results clearly demonstrate reversible CT and magnetic phase switching associated with anisole desorption and re-adsorption, highlighting the dynamic coupling among guest transport, HB modulation, and electronic-state regulation.

Theoretical analysis of the PCCT mechanism

Theoretical analysis is particularly important in this study because the structural differences between the neutral and ionic phases are relatively small. Consequently, experimental structural analysis alone cannot fully explain why CT occurs only after the second desolvation step. In contrast, DFT calculations provide critical insights into how HB disruption modifies the donor potential and cooperatively stabilizes the CT state. The theoretical calculations also allow the separation of contributions from proton displacement and local structural relaxation. Because both effects occur simultaneously during the actual desolvation process, theoretical modeling is necessary to evaluate their individual roles in stabilizing the ionic states.

To elucidate the mechanism of CT during desolvation, DFT calculations were performed using tri-unit cluster models derived from the crystal structures of **1-3Ani** and **1**. Each model consists of [Ru(1)$_2$]–(BTDA-TCNQ)–[Ru(2)$_2$] units (Fig. 5a and Table S8). Four charge–spin states were considered: FM and AFM configurations for the neutral state and FM and ferrimagnetic (FiM) configurations for the CT state, each of which provided an exchange coupling (J) between the nearest-neighbor spin units. Thus, the relative stabilities of the four charge–spin states were evaluated. In the neutral state of **1-3Ani**, both [Ru(1)$_2$] and [Ru(2)$_2$] exhibit the oxidation state [$Ru_2^{II,II}$] with S = 1, characterized by the orbital configuration $\sigma^2(2\pi)^4\delta^2\delta^{*2}(2\pi^*)^2\sigma^{*0}$,[47] whereas BTDA-TCNQ remains neutral. Conversely, in the CT state of **1**, [Ru(1)$_2$] and [Ru(2)$_2$] have oxidation states of [$Ru_2^{II,II}$] and [$Ru_2^{II,III}$]$^+$, respectively. The [$Ru_2^{II,III}$]$^+$ state features S = 3/2 with the orbital configuration $\sigma^2(2\pi)^4\delta^2\delta^{*1}(2\pi^*)^2\sigma^{*0}$,[47] and BTDA-TCNQ becomes a monoanionic radical (BTDA-TCNQ$^{\bullet-}$) with S = 1/2.

<<Insert Fig. 5 here>>

First, the total energies and $\langle \widehat{S}^2 \rangle$ values for the four charge–spin states were calculated (Table S9), and their relative energies are presented in Table 1. These calculations reproduced the experimentally observed electronic states of the compounds. The neutral state is the most stable for the **1-3Ani** model, whereas the CT state is favored for the **1** model. For the **1-3Ani** model, the HOMO is localized mainly on the [Ru_2] units and the LUMO on BTDA-TCNQ, reflecting a conventional donor–acceptor relationship (Fig. S11). In contrast, the HOMO-1 orbital of the **1** model exhibits substantial electron density distributed over both BTDA-TCNQ and the oxidized [$Ru(2)_2$]$^+$ unit, directly confirming CT (Fig. S11).

<<Insert Table 1 here>>

For the neutral **1-3Ani** model, the FM and AFM states are nearly degenerate, indicating negligible magnetic exchange through neutral BTDA-TCNQ. In contrast, the CT **1** model strongly favors the FiM state, indicating a strong AFM exchange coupling between [Ru_2]$^{n+}$ and BTDA-TCNQ$^{\bullet-}$. DFT calculations estimated an average exchange interaction of approximately −182 cm^{-1}, which is somewhat larger than the experimentally observed values for related chain systems,[58,59,60] likely owing to the limitations of the cluster model.[61,62]

To identify the trigger for CT, the proton position in the Bz4 ligand of the **1-3Ani** model was systematically rotated to simulate disruption of the HBs (Fig. 5c). The definition of $\Delta\theta$ is consistent with that used for [Ru_2(4-F-2-OHArCO$_2$)$_4$(THF)$_2$] (inset of Fig. 5c), where the original intramolecular HB angle (Bz4: 1.00°) is defined as $\Delta\theta = 0°$ and the other geometric parameters were fixed to the X-ray structure. As the HB disruption angle increased from 0° to 180°, the energy gap (ΔE) between the neutral and CT states decreased significantly (Fig. 5c), demonstrating that ΔE is affected by the HB

mode. However, HB disruption alone was insufficient to fully invert the relative stabilities of the two states. Therefore, we varied two additional structural parameters associated with oxidation-state changes, namely the Ru–N_{ax} ($r_{Ru–N}$) and Ru–O_{eq} ($r_{Ru–O}$) bond distances, from the values observed for **1-3Ani** to those observed for **1** (Fig. 5d and 5e).[63] To examine the relative stability of the CT and neutral states, we compared the most stable spin alignments for each, namely the FiM alignment for the CT state and the FM alignment for the neutral state, as follows:

$$\Delta E = E_{tot}(CT, FiM) - E_{tot}(N, FM).$$

When ΔE is positive, the neutral state is more stable; when ΔE is negative, the CT state is favored. The ΔE values in both $r_{Ru–N}$ and $r_{Ru–O}$ for the original form, i.e., the **1-3Ani** model, are positive, consistent with the data in Table 2. As $r_{Ru–N}$ and $r_{Ru–O}$ extended toward the **1** model, ΔE gradually decreased, reaching its lowest value when $r_{Ru–N}$ and $r_{Ru–O}$ reached the value of the **1** model (Fig. 5d and e).

<<Insert Table 2 here>>

Each of the variations in $\Delta\theta$, Ru–N_{ax} distance, and Ru–O_{eq} distance stabilizes the CT state by approximately 2–5 kcal mol^{-1} (Fig. 5d and e), but no single parameter induces a complete crossover between the neutral and CT states in the cluster models for calculations. In contrast, the simultaneous variation of all parameters causes the CT state to become more stable than the neutral state by approximately 2.3 kcal mol^{-1} even in the model. These calculations demonstrate that disruption of the intramolecular HB elevates the donor HOMO energy level, while the accompanying local structural relaxation cooperatively stabilizes the ionic state, ultimately inducing the CT transition.

Discussion

We show the direct demonstration of proton-coupled CT in a redox-active layered MOF, in which modulation of intramolecular HBs governs CT in the framework and the magnetic phase

transformation. A layered D_2A-MOF, composed of *o*-OH-substituted benzoate-bridged paddlewheel diruthenium donors and BTDA-TCNQ acceptors, initially adopts a neutral PM state because the donor HOMO level lies below the acceptor LUMO level. Stepwise desolvation disrupts the intramolecular HBs in one [Ru_2] unit, increasing its donor ability and promoting a one-electron transfer to BTDA-TCNQ. The resulting ionic state generates ferrimagnetic layers exhibiting long-range AFM ordering with T_N = 58 K. Structural analyses revealed only minor framework rearrangements during desolvation, indicating that the CT process is primarily driven by intrinsic modulation of the donor potential through HB disruption rather than by large-scale structural transformation. DFT calculations confirmed that HB cleavage raised the donor HOMO level and, together with local bond relaxation, stabilized the CT state.

This work represents the first MOF system in which modulation of intramolecular HB modes explicitly controls the framework CT and triggers a magnetic phase transformation. These findings establish a new PCCT mechanism activated by an external chemical stimulus, providing a strategy for designing responsive magnetic and electronic materials through proton and HB engineering.

Methods

Synthesis of materials. All synthetic procedures were carried out under an inert atmosphere using standard Schlenk line techniques and commercial glove boxes. All chemicals were purchased from commercial sources and were of reagent grade. Before use, the solvents were distilled using a common drying agent under an N_2 atmosphere. The starting materials, $[Ru_2^{II,II}(4\text{-F-2-OHArCO}_2)_4(THF)_2]$[42] and BTDA-TCNQ,[64] were synthesized according to previously reported procedures.

Synthesis of 1-3Ani. An anisole solution (10 mL) of $[Ru_2^{II,II}(4\text{-F-2-OHArCO}_2)_4(THF)_2]$ (38 mg, 0.04 mmol) was separated into five 2-mL portions and placed at the bottom of narrow glass tubes with a diameter of 8 mm. A mixed solvent of anisole and benzene (1:1 v/v, 1 mL) was then added onto the bottom layer as a buffer layer. Finally, a 2-mL aliquot of a BTDA-TCNQ solution in benzene

(6.4 mg, 0.02 mmol, in 10 mL benzene) was carefully placed on the buffer layer of each tube as the top layer. The glass tubes were left undisturbed for one week, yielding block-shaped dark-brown crystals of **1-3Ani** (yield: 48%). TG measurements indicated that the crystals contained crystallization solvents (3 moles of anisole per formula unit), which matched well with the elemental analysis results ($C_{89}H_{56}F_8N_8O_{27}Ru_4S_2$: C, 46.64; H, 2.45; N, 4.89. Found: C, 46.69; H, 2.48; N, 5.15). IR (KBr): ν(C≡N), 2223, 2196 cm^{-1}.

Preparation of 1-2Ani. A crystalline sample of **1-3Ani** was heated at 373 K under vacuum for 12 h. Elemental analysis for $C_{82}H_{48}F_8N_8O_{26}Ru_4S_2$: C, 45.14; H, 2.24; N, 5.14. Found: C, 44.76; H, 2.51; N, 5.26. IR (KBr): ν(C≡N), 2224, 2198 cm^{-1}.

Preparation of 1. A crystalline sample of **1-3Ani** was heated at 393 K under vacuum for 12 h. Elemental analysis for $C_{68}H_{32}F_8N_8O_{24}Ru_4S_2$: C, 41.52; H, 1.63; N, 5.70. Found: C, 40.74; H, 1.86; N, 5.71. IR (KBr): ν(C≡N), 2197, 2170 cm^{-1}.

Preparation of 1-reAni. After soaking in a 1:1 (v/v) hexane/anisole mixture at 298 K for one week, compound **1** adsorbed 3 molar amounts of anisole, forming **1-reAni**. PXRD and SCXRD analyses of **1-reAni** revealed that it was isostructural with **1-3Ani** (Fig. S4).

Characterization. FT-IR spectra were recorded using KBr pellets on a JASCO FT-IR 4200 spectrometer. Raman spectra were collected from a single crystal using a JASCO NRS-4500 Raman microscope equipped with a 532 nm excitation laser and an Olympus M PLAN 100× objective lens. TG analyses were conducted on a Shimadzu DTG-60H apparatus under an N_2 atmosphere in the temperature range of 298−673 K at a heating rate of 5 K min^{-1}. PXRD patterns were collected with 0.02° steps on a Rigaku Ultima IV diffractometer with Cu Kα radiation (λ = 1.5418 Å) using a θ scan. Magnetic measurements were conducted using a Quantum Design SQUID magnetometer (MPMS-XL) with temperature and DC field ranges of 1.8–300 K and −7 to 7 T, respectively. AC measurements were performed at different frequencies ranging from 1 to 1488 Hz under an AC field amplitude of 3 Oe and no DC field. Polycrystalline samples embedded in Nujol were analyzed. The diamagnetic contributions of the sample holder, Nujol, and sample were estimated using Pascal constants.[65]

***In situ* PXRD measurements.** A ground sample of **1-3Ani** was sealed in a silica glass capillary with an inner diameter of 0.5 mm. PXRD patterns were obtained with 0.02° steps using a diffractometer (Rigaku Ultima IV) with Cu Kα radiation (λ = 1.5418 Å) and a θ scan. The glass capillary was connected to stainless-steel lines with valves, which were connected to a gas-handling system (BELSORP MINI X; Microtrac-BEL). Temperature was controlled using an N_2 gas stream.

Crystallography. Crystal data for **1-3Ani**, **1-2Ani**, **1**, and **1-reAni** were collected using a Rigaku Hypix 6000 hybrid photon-counting X-ray detector with multilayer mirror-monochromated Mo Kα radiation (λ = 0.71075 Å). Single crystals were mounted on a thin Kapton film using Nujol and cooled to 102 K under an N_2 stream. Using Olex2,[66] the structure was solved with the SHELXT (version 2018/2)[67] program using Intrinsic Phasing, and then refined with the SHELXL (version 2018/3)[67] package using least-squares minimization. Anisotropic refinement of the non-hydrogen atoms was performed using the full-matrix least-squares method on F^2. Hydrogen atoms were treated using standard SHELXL procedures. H atoms attached to carbon atoms were placed in geometrically calculated positions using the HADD command and refined with a riding model. For hydroxy groups relevant to the hydrogen-bonding modes, the H-atom orientations were assigned using a free rotation treatment, guided by residual electron-density peaks in the difference-Fourier map when available. In some disordered regions of compound **1**, where no reliable residual electron density peaks attributable to hydrogen atoms were observed, the hydroxy H atoms (H3A for Bz1 and H12A for Bz4) were positioned based on standard O–H distances, local hydrogen-bonding geometry, and potential acceptor atoms. In the final refinement, all H atoms were included as fixed contributions. The crystallographic data are summarized in Table S2. The CIF data for **1-3Ani**, **1-3Ani**, **1**, and **1-reAni** have been deposited at the Cambridge Crystallographic Data Centre as Supplementary Publication Nos. CCDC-2570565, 2570566, 2570567, and 2570568, respectively. Structural diagrams were prepared using the VESTA[68] and Diamond[69] software.

DFT calculations for H-rotated [Ru_2] models in [Ru_2(4-F-2-OHArCO$_2$)$_4$(THF)$_2$]. *Ab initio* calculations were performed using the DFT formalism implemented in Gaussian 16,[70] employing

Becke's three-parameter hybrid functional in combination with the Lee–Yang–Parr correlation functional (B3LYP).[71] Unrestricted open-shell calculations were performed for the molecules containing [Ru_2] units. The effective core potential basis function LanL2TZ with polarization (LanL2TZ(f))[72,73,74] was used for Ru atoms, whereas the 6-31G basis sets with polarization and diffusion functions (6-31+G(d))[75,76,77,78,79] were used for C, H, F, and O atoms. Spin polarization with S_Z = 1 (triplet spin multiplicity) was used for the [Ru_2] units. The atomic coordinates determined by X-ray crystallography were used in the calculations.

DFT calculations for the tri-unit models of 1-3Ani and 1. The model structures of **1-3Ani** and **1** were constructed based on the coordinates obtained from X-ray crystallographic analyses and contained two [Ru_2] and one BTDA-TCNQ units. The Cartesian coordinates of the **1-3Ani** and **1** models are summarized in Table S9. Spin-unrestricted density functional theory (UDFT) calculations were performed on these models using B3LYP. The basis functions employed were LANL08(f) for Ru and 6-31G* for all other atoms. All calculations were performed in the gas phase using Gaussian 09 rev. D01.[80]

Data availability

The data supporting the findings of this study are available within the paper and the Supplementary Information. The source data underlying the figures have been deposited in Figshare at XXXXXXXXXXXXXX.

Acknowledgements

This study was supported by MEXT/JSPS KAKENHI (Grant Nos. JP23K21104, JP20H00381, JP23K17899, JP24H00459, JP25K22264, JP26K01476, and JP26H02280) and by the GIMRT and E-IMR projects at the Institute for Materials Research, Tohoku University (Proposal No. 202603-RDKGE-0058). This work was partially supported by the JSPS Bilateral Program No. JPJSBP120267406. K.J. gratefully acknowledges financial support from the Chinese Scholarship

Council (CSC).

Author information

Contributions

H.M. conceived and designed the study. K.J. and C.I. synthesized the compounds and conducted materials characterization with the support of H.Y. K.J. performed the experiments and analyzed the data. W.K. contributed to DFT calculations of the units, magnetic measurements, and discussions regarding the correlation between structure, electronic states, and magnetic properties. R.N., K.T., R.I., and Y.K. performed the DFT calculations for the tri-unit models and contributed to discussions of the results. K.J., Y.K., and H.M. wrote the manuscript. All authors contributed to the editing of the final manuscript.

Corresponding authors

Correspondence to Hitoshi Miyasaka.

Ethics declarations

Competing interests

The authors declare no competing interests.

Supplementary information

Source data

Rights and permissions

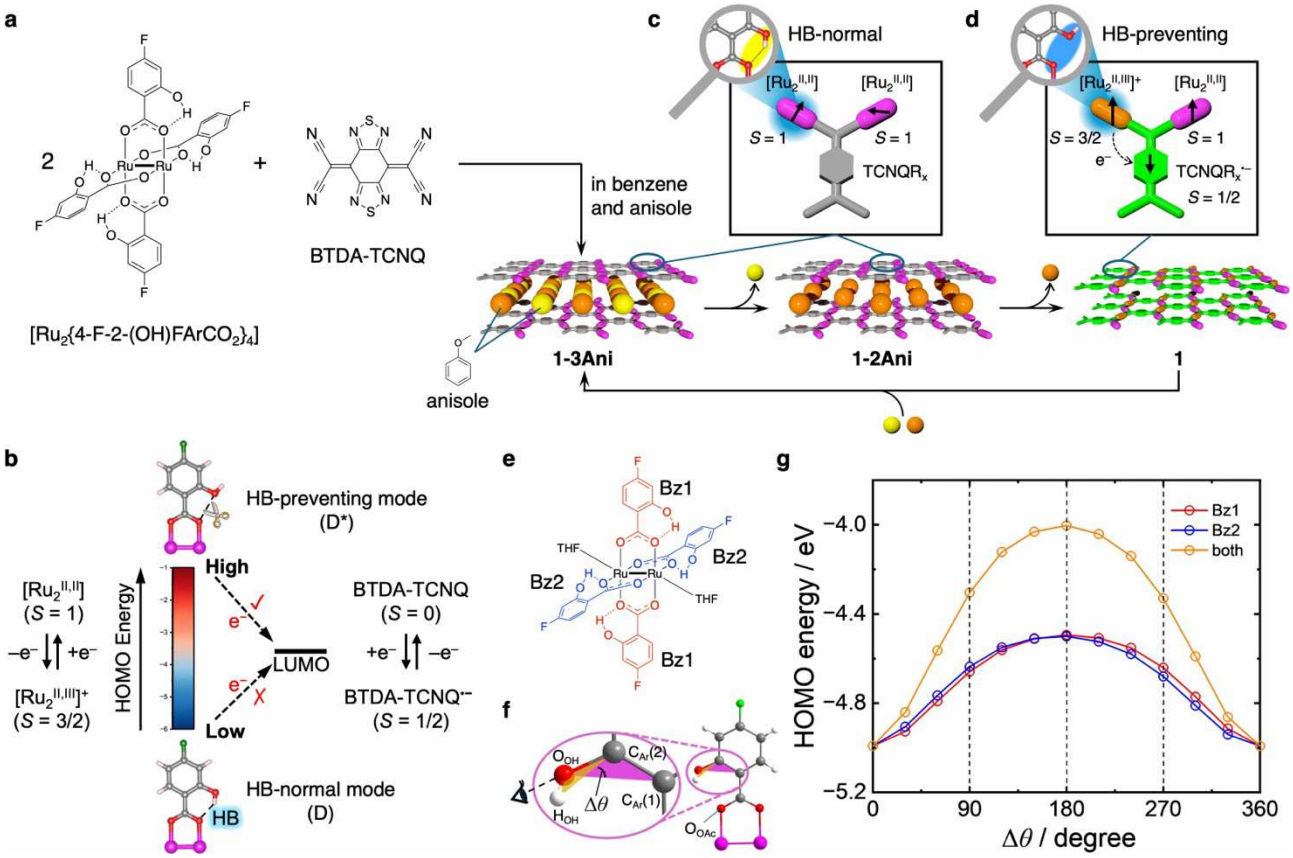


Fig. 1 | Material variations and the relationship between charge transfer (CT) and intramolecular hydrogen bonding. a Reaction scheme of $[Ru_2(4\text{-F-2-OHArCO}_2)_4]$ as the D unit and BTDA-TCNQ as the A unit, together with the arrangement of layered D_2A-MOFs during the stepwise desolvation and resolvation processes. **b** Schematic representation of CT tuned by modulating the electron-donor character *via* protonation/deprotonation or by modifying hydrogen bonds (HBs) in the framework. Disruption of intramolecular HBs elevates the HOMO level of D, providing D*. **c** Schematic diagrams of the charge distribution, spin arrangement, and intramolecular hydrogen bonding in **1-3Ani** and **1-2Ani**. **d** Schematic diagrams of the charge distribution, spin arrangement, and intramolecular hydrogen bonding in **1**. **e** A homoleptic series of $[Ru_2(4\text{-F-2-OHArCO}_2)_4(THF)_2]$, where an inversion center is located at the midpoint of the Ru–Ru bond. **f** Diagram of hydrogen atom rotation around the Ar–O bond axis. Rotation is described by the relative dihedral angle $\Delta\theta$ formed between the plane defined by C_{Ar}–C_{Ar}–O and the plane defined by C_{Ar}–O–H in the Ar–O–H group. The C, O, H, F, and Ru atoms are colored in gray, red, white, green, and pink, respectively. **g** Plots of HOMO energy *versus* $\Delta\theta$ for the homoleptic series of $[Ru_2(4\text{-F-2-OHArCO}_2)_4(THF)_2]$.

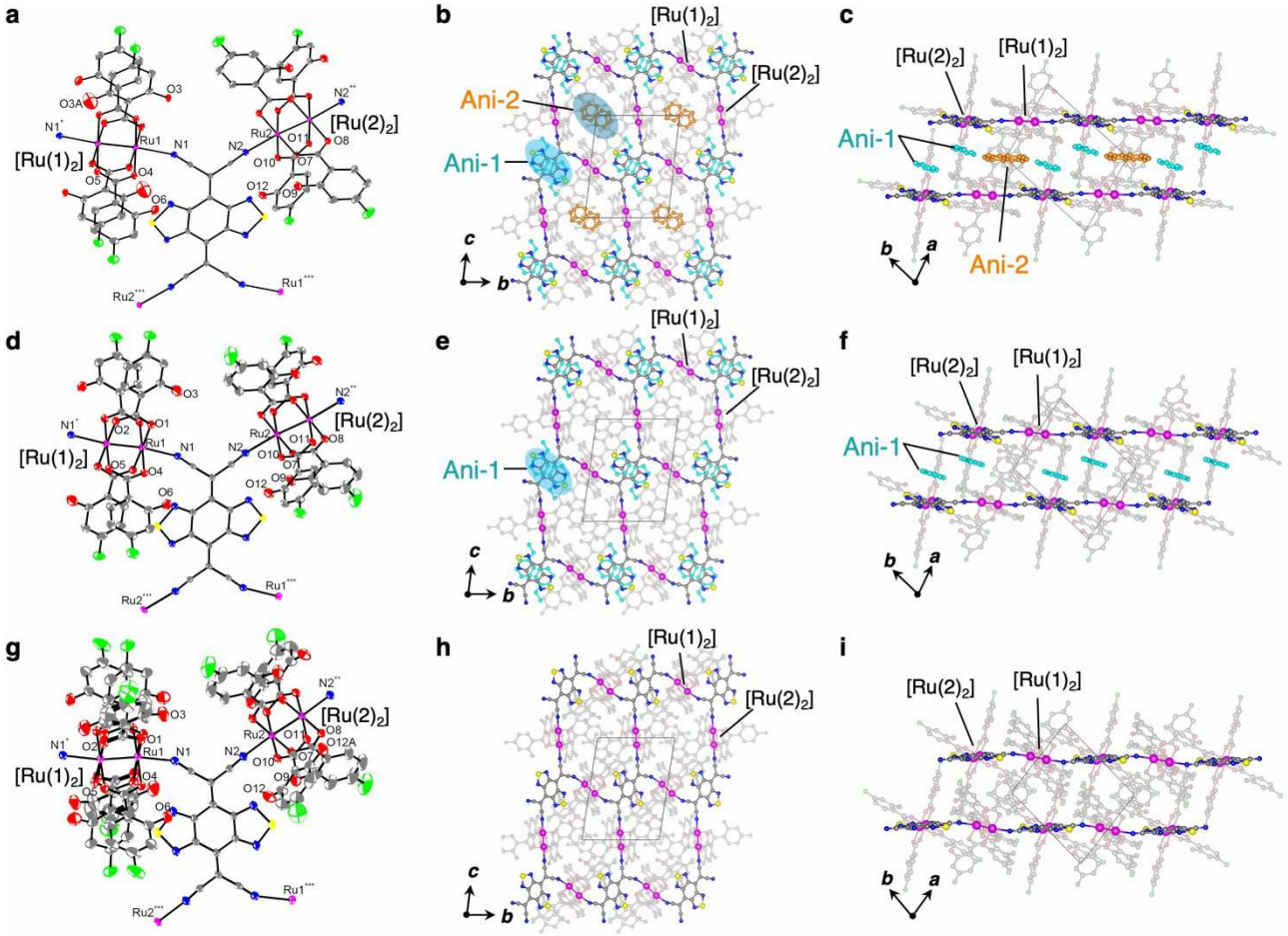


Fig. 2 | Structures of 1-3Ani (a–c), 1-2Ani (d–f), and 1 (g–i). a, d, g The asymmetric unit [Ru(1)$_2$]–(BTDA-TCNQ)–[Ru(2)$_2$], where crystallization solvent molecules (anisole) and hydrogen atoms are omitted for clarity. **b, e, h** Packing views projected along the *a*-axis. **c, f, i** Packing views projected along the *c*-axis. The C, N, S, and Ru atoms are represented in gray, blue, yellow, and pink, respectively. Anisole molecules with different packing modes (Ani-1 and Ani-2) are shown in cyan and orange, respectively, and hydrogen atoms are omitted for clarity.

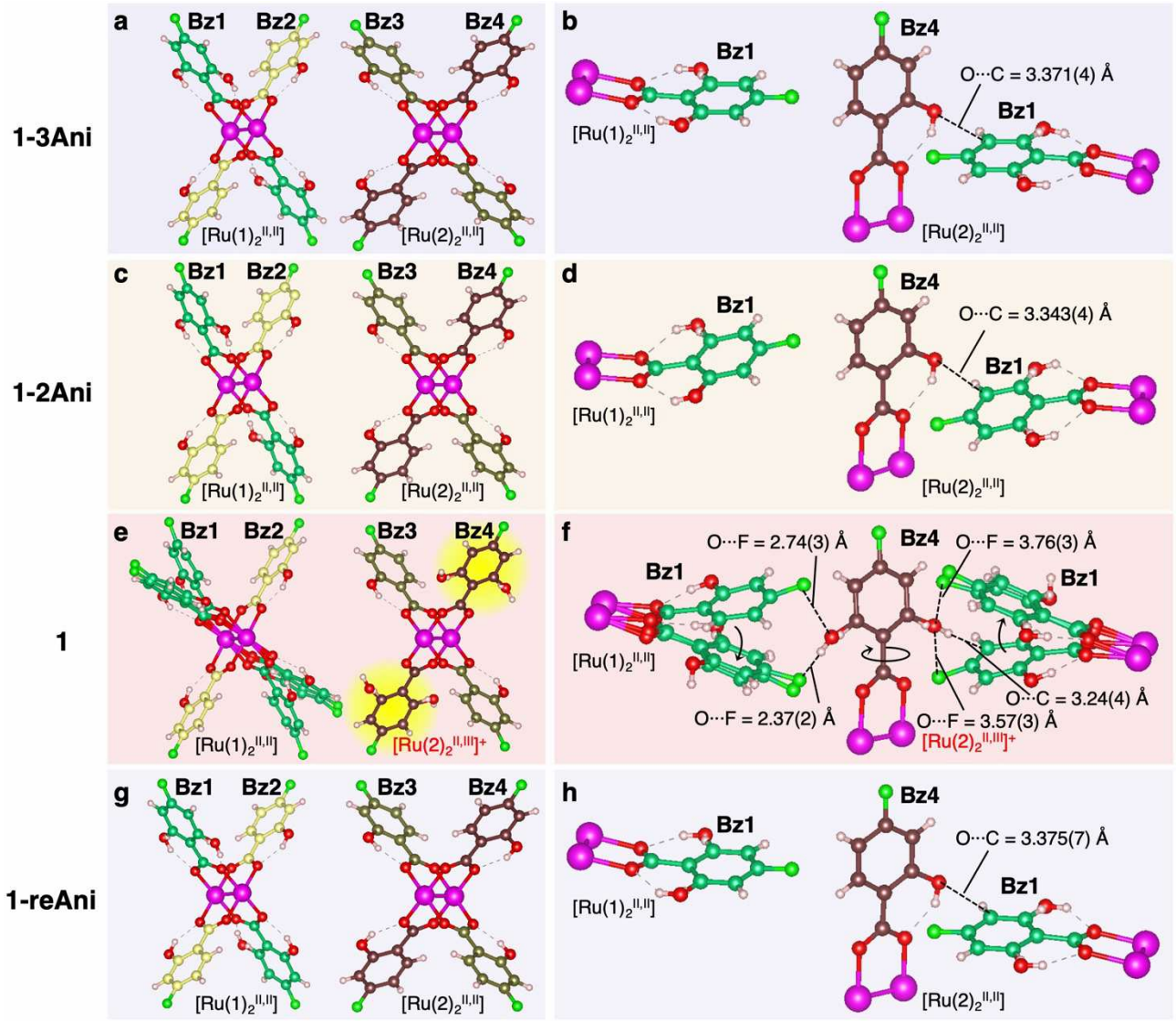


Fig. 3 | Diagrams of intramolecular HB modes and packing environments in 1-3Ani, 1-2Ani, 1, and 1-reAni. a, c, e, g Close-up views of the [Ru(1)$_2$] and [Ru(2)$_2$] moieties showing variations in the HB modes. Only the HBs in Bz4 of **1** are disrupted and disordered, as marked in yellow circles. **b, d, f, h** Packing environments around the [Ru(2)$_2$] subunit, showing variations in HBs during the desolvation/solvation processes. The diagram in **f** represents the disordering modes of Bz1 and Bz4. The C, O, F, and Ru atoms are colored in gray, red, green, and pink, respectively. The C atoms on Bz1, Bz2, Bz3, and Bz4 are colored in pale green, pale yellow, olive, and brown, respectively.

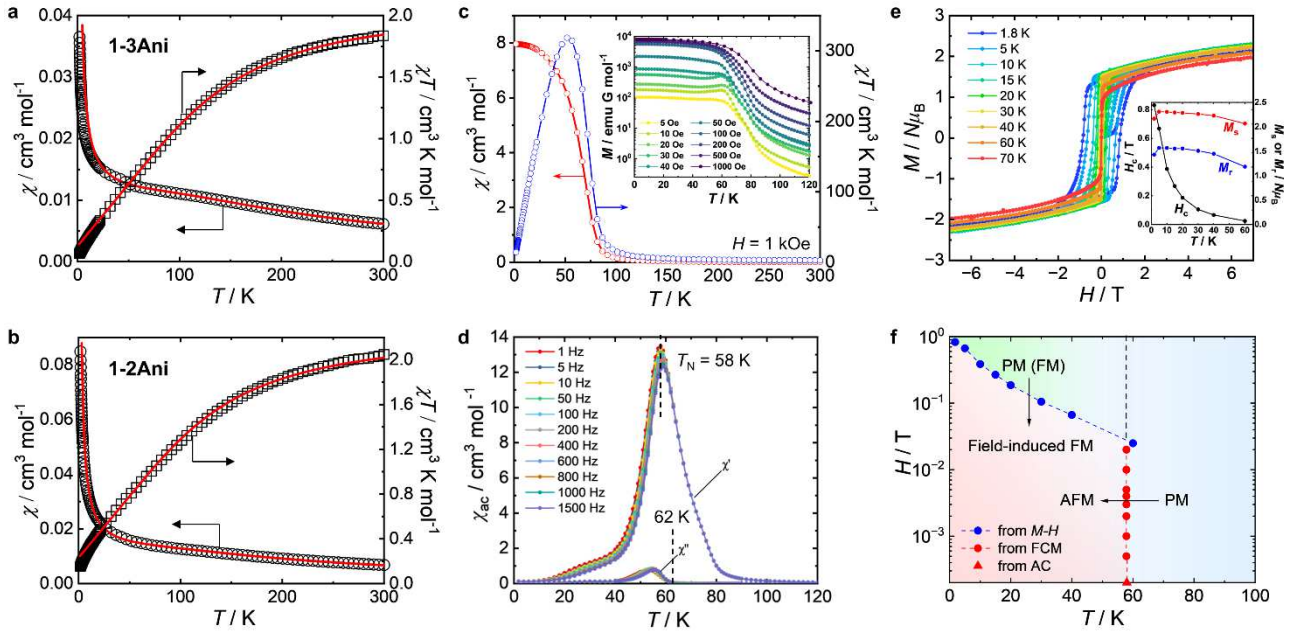


Fig. 4 | Magnetic properties of 1-3Ani, 1-2Ani, and 1. a Temperature dependence of χ_M (open circles) and $\chi_M T$ (open squares) measured under a DC field of 1 kOe for **1-3Ani**. **b** Temperature dependence of χ_M (open circles) and $\chi_M T$ (open squares) measured under a DC field of 1 kOe for **1-2Ani**. **c** Temperature dependence of the DC susceptibility χ and χT product measured during cooling under a field of 1 kOe for **1**. Inset: field-cooled magnetization (FCM) curves measured at different external fields from 5 Oe to 1 kOe. **d** Temperature dependence of the AC susceptibilities χ' (in-phase) and χ'' (out-of-phase) under zero DC field and a 3 Oe AC oscillating field for **1**. **e** Field dependence of magnetization at several temperatures between 1.8 and 90 K for **1**. Inset: temperature dependence of the coercive field (H_c), saturated magnetization (M_s), and remnant magnetization (M_r). **f** H–T phase diagram of **1**, where AFM, PM, and FM represent the antiferromagnetic, paramagnetic, and ferromagnetic phases, respectively, and the arrow from the FM to the AFM phase represents the field-induced ferromagnetic transition.

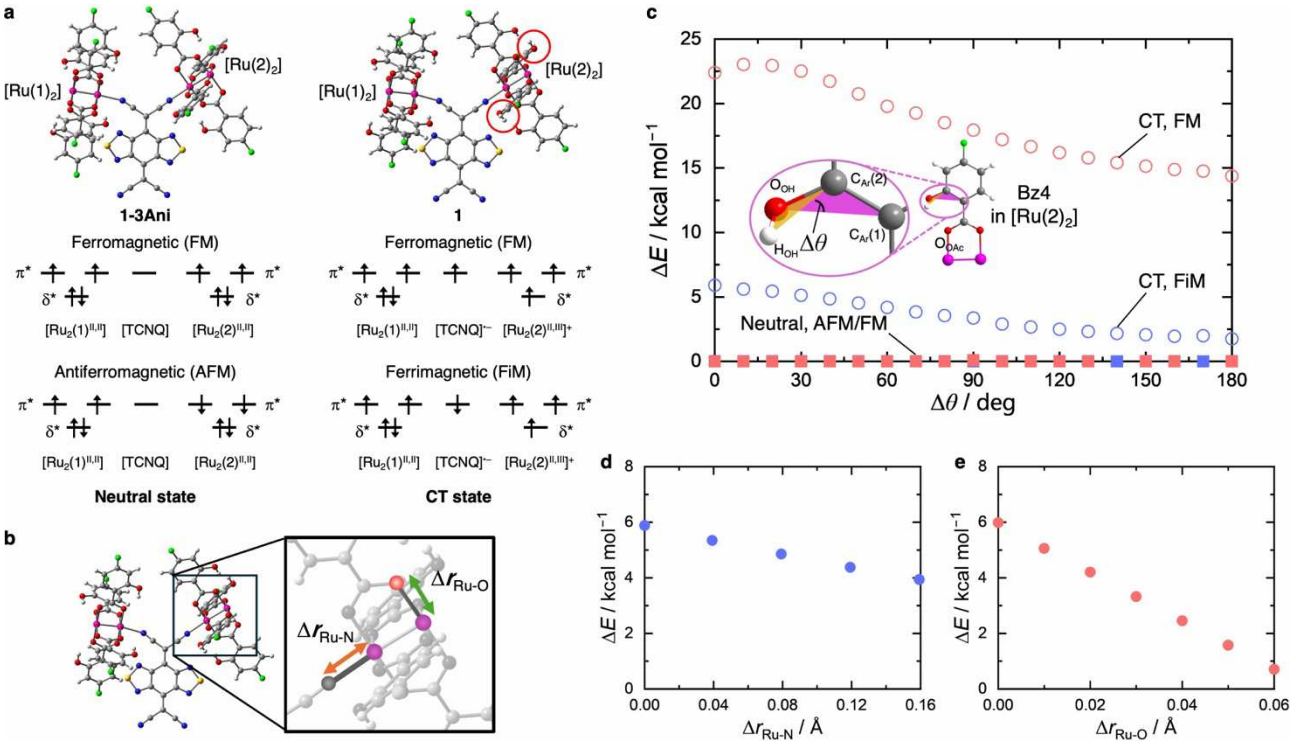


Fig. 5 | DFT calculations of the three-unit model of [Ru(1)$_2$]–(BTDA-TCNQ)–[Ru(2)$_2$]. a Illustration of the model structures of **1-3Ani** and **1** and their charge-spin states as neutral and CT states, respectively, where the red circles in the [Ru(2)$_2$] moiety indicate free O–H groups resulting from HB dissociation. **b** Illustration of the models with modified bond lengths, where $r_{Ru–N}$ and $r_{Ru–O}$ are varied in the ranges of 0–0.16 and 0–0.06 Å, respectively. **c** Energy variations associated with HB rotation, where the horizontal axis represents the HB dihedral angle (θ) of the Bz4 moiety in the [Ru(2)$_2$] subunit. **d** Plots of ΔE vs. $\Delta r_{Ru–N}$. **e** Plots of ΔE vs. $\Delta r_{Ru–O}$.

Table 1. Relative energies (kcal mol^{-1}) of the four charge–spin states. The energy of the most stable ferromagnetic (FM) state in the neutral **1-3Ani** model was set to zero as the reference.

Charge State	Neutral state		CT state	
	AFM state	FM state	FiM state	FM state
1-3Ani	0.1	0.0	2.3	15.8
1	63.7	62.8	62.1	62.9

Table 2. Differences in the major structural parameters between **1-3 Ani** and **1**.

X-ray Structure	H-bond dihedral angle [˚]	$r_{Ru–N}$ [Å]	$r_{Ru–O}$ [Å]
1-3 Ani	0.0	2.22	2.02
1	74.0	2.36	2.07

References

(1) Tyburski, R.; Liu, T.; Glover, S. D. & Hammarström, L. Proton-coupled electron transfer guidelines, fair and square. *J. Am. Chem. Soc.* **143**, 560–576 (2021).

(2) Weinberg, D. R. et al. Proton-coupled electron transfer. *Chem. Rev.* **112**, 4016–4093 (2012).

(3) Reece, S. Y. & Nocera, D. G. Proton-coupled electron transfer in biology: results from synergistic studies in natural and model systems. *Annu. Rev. Biochem.* **78**, 673–699 (2009).

(4) Dempsey, J. L.; Winkler, J. R. & Gray, H. B. Proton-coupled electron flow in protein redox machines. *Chem. Rev.* **110**, 7024–7039 (2010).

(5) Migliore, A.; Polizzi, N. F.; Therien, M. J. & Beratan, D. N. Biochemistry and theory of proton-coupled electron transfer. *Chem. Rev.* **114**, 3381–3465 (2014).

(6) Ishikita, H. & Knapp, E.-W. Control of quinone redox potentials in photosystem II: electron transfer and photoprotection. *J. Am. Chem. Soc.* **127**, 14714–14720 (2005).

(7) Kaila, V. R. I. Resolving chemical dynamics in biological energy conversion: long-range proton-coupled electron transfer in respiratory complex I. *Acc. Chem. Res.* **54**, 4462–4473 (2021).

(8) Wada, K. et al. Protonation/deprotonation-driven switch for the redox stability of low-potential [4Fe-4S] ferredoxin. *eLife* **13**:RP102506 (1-26) (2024).

(9) Mori, H.; Yokomori, S.; Dekura, S. & Ueda, A. Proton–electron-coupled functionalities of conductivity, magnetism, and optical properties in molecular crystals. *Chem. Commun.* **58**, 5668–5682 (2022).

(10) Ueda, A. et al. Hydrogen-bond-dynamics-based switching of conductivity and magnetism: a phase transition caused by deuterium and electron transfer in a hydrogen-bonded purely organic conductor crystal. *J. Am. Chem. Soc.* **136**, 12184–12192 (2014).

(11) Nakanishi, T. et al. Observation of proton transfer coupled spin transition and trapping of photoinduced metastable proton transfer state in an Fe(II) complex. *J. Am. Chem. Soc.* **141**, 14384–14393 (2019).

(12) Tadokoro, M. et al. Synchronized collective proton-assisted electron transfer in solid state by hydrogen-bonding Ru(II)/Ru(III) mixed-valence molecular crystals. *Inorg. Chem.* **56**, 8513–8526 (2017).

(13) Kitagawa, S., Kitaura, R. & Noro, S. Functional porous coordination polymers. *Angew. Chem. Int. Ed.* **43**, 2334–2375 (2004).

(14) Horike, S., Shimomura, S. & Kitagawa, S. Soft porous crystals. *Nat. Chem.* **1**, 695–704 (2009).

(15) Férey, G. & Serre, C. Large breathing effects in three-dimensional porous hybrid matter: facts,

analyses, rules and consequences. *Chem. Soc. Rev.* **38**, 1380–1399 (2009).

(16) Schneemann, A. et al. Flexible metal–organic frameworks. *Chem. Soc. Rev.* **43**, 6062–6096 (2014).

(17) Allendorf, M. D. et al. Guest-induced emergent properties in metal–organic frameworks. *J. Phys. Chem. Lett.* **6**, 1182–1195 (2015).

(18) Yanai, N. et al. Gas detection by structural variations of fluorescent guest molecules in a flexible porous coordination polymer. *Nat. Mater.* **10**, 787–793 (2011).

(19) Kreno, L. E. et al. Metal–organic framework materials as chemical sensors. *Chem. Rev.* **112**, 1105–1125 (2012).

(20) Coronado, E. & Mínguez Espallargas, G. Dynamic magnetic MOFs. *Chem. Soc. Rev.* **42**, 1525–1539 (2013).

(21) Mínguez Espallargas, G. & Coronado, E. Magnetic functionalities in MOFs: from the framework to the pore. *Chem. Soc. Rev.* **47**, 533–557 (2018).

(22) Halder, G. J., Kepert, C. J., Moubaraki, B., Murray, K. S. & Cashion, J. D. Guest-dependent spin crossover in a nanoporous molecular framework material. *Science* **298**, 1762–1765 (2002).

(23) Murphy, M. J. et al. Guest programmable multistep spin crossover in a porous 2-D Hofmann-type material. *J. Am. Chem. Soc.* **139**, 1330–1335 (2017).

(24) Zhang, J., Kosaka, W., Kitagawa, Y. & Miyasaka, H. A metal–organic framework that exhibits CO_2-induced transitions between paramagnetism and ferrimagnetism. *Nat. Chem.* **13**, 191–199 (2021).

(25) Zhang, J. et al. Magnetic Sponge Behavior via Electronic State Modulations. *J. Am. Chem. Soc.* **140**, 5644–5652 (2018).

(26) Zhang, J. et al. Host-Guest Hydrogen Bonding Varies the Charge-State Behavior of Magnetic Sponges. *Angew. Chem. Int. Ed.* **58**, 7351–7356 (2019).

(27) Zhang, J. et al. Magnet Creation by Guest Insertion into a Paramagnetic Charge-Flexible Layered Metal-Organic Framework. *J. Am. Chem. Soc.* **143**, 7021–7031 (2021).

(28) Kosaka, W. et al. Densely Packed CO_2 Aids Charge, Spin, and Lattice Ordering Partially Fluctuated in a Porous Metal-Organic Framework Magnet. *Angew. Chem. Int. Ed.* **62**, e202312205 (2023).

(29) Zhang. J. et al. CO_2-Sensitive Porous Magnet: Antiferromagnet Creation from a Paramagnetic Charge-Transfer Layered Metal-Organic Framework. *J. Am. Chem. Soc.* **145**, 26179–26189 (2023).

(30) Saouma, C. T. et al. Bulk-to-surface proton-coupled electron transfer reactivity of the metal–

organic framework MIL-125. *J. Am. Chem. Soc.* **140**, 16184–16189 (2018).

(31) Mancuso, J. L., Fabrizio, K., Brozek, C. K. & Hendon, C. H. On the limit of proton-coupled electronic doping in a Ti(IV)-containing MOF. *Chem. Sci.* **12**, 11779–11785 (2021).

(32) Miyasaka, H. Control of charge transfer in donor/acceptor metal–organic frameworks. *Acc. Chem. Res.* **46**, 248–257 (2013).

(33) Miyasaka, H. Charge manipulation in metal-organic frameworks: Toward designer functional molecular materials. *Bull. Chem. Soc. Jpn.* **94**, 2929–2955 (2021).

(34) Miyasaka, H. et al. Control of charge transfer in a series of $Ru_2^{II,II}$/TCNQ two-dimensional networks by tuning the electron affinity of TCNQ units: a route to synergistic magnetic/conducting materials. *J. Am. Chem. Soc.* **132**, 1532–1544 (2010).

(35) Sekine, Y., Nishio, M., Shimada, T., Kosaka, W. & Miyasaka, H. Ionicity diagrams for electron-donor and -acceptor metal–organic frameworks: DA chains and D_2A layers obtained from paddlewheel-type diruthenium(II,II) complexes and polycyano-organic acceptors. *Inorg. Chem.* **60**, 3046–3056 (2021).

(36) Fukunaga, H. et al. Charge-disproportionate ordered state with $\delta = 0.75$ in a chemically sensitive donor/acceptor $D^{\delta+}{}_2A^{2\delta-}$ layered framework. *Chem. Commun.* **51**, 7795–7798 (2015).

(37) Kosaka, W., Morita, T., Yokoyama, T., Zhang, J. & Miyasaka, H. Fully electron-transferred donor/acceptor layered frameworks with $TCNQ^{2-}$. *Inorg. Chem.* **54**, 1518–1527 (2015).

(38) Kosaka, W. et al. Gas-responsive porous magnet distinguishes the electron spin of molecular oxygen. *Nat. Commun.* **9**, 5420 (2018).

(39) Zhang, J., Cao, Y., Kosaka, W. & Miyasaka, H. Guest-Triggered Charge Transfer for Magnetic Change in Redox-Active MOF Magnets. *Acc. Chem. Res.* **59**, 1632–1643 (2026).

(40) Kosaka, W., Watanabe, Y., Aliyah, K. H. & Miyasaka, H. Role of intramolecular hydrogen bonding in the redox chemistry of hydroxybenzoate-bridged paddlewheel diruthenium(II,II) complexes. *Dalton Trans.* **51**, 85–94 (2022).

(41) Kosaka, W., Watanabe, Y., Itoh, C. & Miyasaka, H. High stabilization of low valency in a homoleptic ortho-hydroxybenzoate-bridged paddlewheel diruthenium(II,II) complex. *Chem. Lett.* **51**, 731–734 (2022).

(42) Kosaka, W., Watanabe, Y., Kitayama, T., Itoh, C. & Miyasaka, H. Introduction of substituents for tuning the redox properties of benzoate-bridged paddlewheel diruthenium(II,II) complexes: what does the OH group bring? *Dalton Trans.* **54**, 1838–1849 (2025).

(43) Yamashita, Y., Suzuki, T., Saito, G., & Mukai, T. Highly conductive complexes of bis-1,2,5-thiadiazolo-tetracyanoquinodimethan (BTDA-TCNQ) with amines. *Chem. Lett.* **14**, 1759–1762

(1985)

(44) Suzuki, T. et al. Clathrate formation and molecular recognition by novel chalcogen–cyano interactions in tetracyanoquinodimethanes fused with thiadiazole and selenadiazole rings. *J. Am. Chem. Soc.* **114**, 3034–3043 (1992).

(45) Zhang, J., Kosaka, W., Kitagawa, Y. & Miyasaka, H. A Host–Guest Electron Transfer Mechanism for Magnetic and Electronic Modifications in a Redox-Active Metal–Organic Framework. *Angew. Chem. Int. Ed.* **61**, e202115976 (1-9) (2022).

(46) Taniguchi, K., Narushima, K., Mahin, J., Kosaka, W. & Miyasaka, H. Construction of an artificial ferrimagnetic lattice by lithium ion insertion into a neutral donor/acceptor metal–organic framework. *Angew. Chem. Int. Ed.* **55**, 5238–5242 (2016).

(47) Cotton, F. A. & Walton, R. A. Multiple Bonds Between Metal Atoms, 2nd ed. *Oxford Univ. Press*, *Oxford* **9** (1993).

(48) Kistenmacher, T. J., Emge, T. J., Bloch, A. N. & Cowan, D. O. Structure of the red, semiconducting form of 4,4′,5,5′-tetramethyl-$\Delta^{2,2'}$-bi-1,3-diselenole-7,7,8,8-tetracyano-*p*-quinodimethane, TMTSF–TCNQ. *Acta Crystallogr. Sect. B* **38**, 1193–1199 (1982).

(49) Motokawa, N., Miyasaka, H., Yamashita, M. & Dunbar, K. R. An Electron-Transfer Ferromagnet with T_c = 107 K Based on a Three-Dimensional $[Ru_2]_2$/TCNQ System. *Angew. Chem. Int. Ed.* **47**, 7760–7763 (2008).

(50) Di Mino, C. et al. Strong structuring arising from weak cooperative O–H···π and C–H···O hydrogen bonding in benzene–methanol solution. *Nat. Commun.* **14**, 5900 (2023).

(51) Miyasaka, H., Clérac, R., Campos-Fernández, C. S. & Dunbar, K. R. The first crystal structure of a one-dimensional chain of linked Ru^{II}=Ru^{II} units. *J. Chem. Soc., Dalton Trans.* 858–861 (2001).

(52) Dikarev, E. V., Filatov, A. S., Clérac, R. & Petrukhina, M. A. Unligated diruthenium(II,II) tetra(trifluoroacetate): the first X-ray structural study, thermal compressibility, Lewis acidity and magnetism. *Inorg. Chem.* **45**, 744–751 (2006).

(53) Nakabayashi, K., Nishio, M., Kubo, K., Kosaka, W. & Miyasaka, H. An ionicity diagram for the family of $[\{Ru_2(CF_3CO_2)_4\}_2(TCNQR_x)]$ ($TCNQR_x$ = R-substituted 7,7,8,8-tetracyano-*p*-quinodimethane). *Dalton Trans.* **41**, 6072–6074 (2012).

(54) Taniguchi, K. et al. In situ reversible ionic control for nonvolatile magnetic phases in a donor/acceptor metal–organic framework. *Adv. Funct. Mater.* **27**, 1604990 (2017).

(55) Ortega-San Martin, L., Chapman, J. P., Lezama, L., Saiz Garitaonandia, J. J., Sánchez Marcos, J., Rodríguez-Fernández, J., Arriortua, M. I. & Rojo, T. Spin-Glass Behaviour in the Double

Perovskite "Sr_2FeTeO_6 " Due to Mis-Site Disorder and Cation Vacancy Formation. *J. Mater. Chem.* **16**, 66–76 (2006).

(56) Lago, J., Blundell, S. J., Eguia, A., Jansen, M. & Rojo, T. Three-Dimensional Heisenberg Spin-Glass Behavior in $SrFe_{0.90}Co_{0.10}O_{3.0}$. *Phys. Rev. B* **86**, 064412 (2012).

(57) Kosaka, W., Liu, Z. & Miyasaka, H. Layered ferrimagnets constructed from charge-transferred paddlewheel [Ru_2] units and TCNQ derivatives: the importance of interlayer translational distance in determining magnetic ground state. *Dalton Trans.* **47**, 11760–11768 (2018).

(58) Miyasaka, H. et al. Stepwise Neutral-Ionic Phase Transitions in a Covalently-Bonded Donor/Acceptor Chain Compound. *J. Am. Chem. Soc.* **133**, 5338–5345 (2011).

(59) Nishio, M. & Miyasaka, H. Magnetic sponge phenomena associated with interchain dipole–dipole interactions in a series of ferrimagnetic chain compounds doped with minor diamagnetic species. *Inorg. Chem.* **53**, 4716–4723 (2014).

(60) Ji, K., Kosaka, W., & Miyasaka, H. Magnetostructural Correlations in Charge Transfer Ionic Chains Derived from Assembly of Paddlewheel Diruthenium(II, II) Complexes and 7,7,8,8-Tetracyano-*p*-quinodimethane Derivatives. *Cryst. Growth Des.* **25**, 6745–6753 (2025).

(61) Kitagawa, Y., Nakanishi, Y., Kataoka, Y., Saito, T., Yasuda, N., Kawakami, T., Yamanaka, S., Okumura, M. & Yamaguchi, K. Theoretical study of intra- and inter-chain magnetic interactions in $[Ni(chxn)_2Br]Br_2$, *Polyhedron* **30**, 3116–3120 (2011).

(62) Amamizu, N., Tada, K., Kishi, R., Kosaka, W., Miyasaka, H. & Kitagawa, Y. Difference in spin structure of magnetic metal-organic frameworks between cluster model and periodic system, *Chem. Lett.* **53**, upae230 (2024).

(63) Cotton, F. A., Matusz, M. & Zhong, B. Oxidation states available to the Ru_2^{n+} core in tetracarboxylato-bridged species. *Inorg. Chem.* **27**, 4368–4372 (1988).

(64) Yamashita, Y.; Suzuki, T.; Mukai, T. *The chemical Society of Japan* **1986***, 3, 268−275.*

(65) Bain, G. A.; Berry, J. F. Diamagnetic Corrections and Pascal's Constants. *J. Chem. Educ.* **2008**, *85* (4), 532.

(66) Dolomanov, O. V.; Bourhis, L. J.; Gildea, R. J.; Howard, J. a. K.; Puschmann, H. OLEX2: A Complete Structure Solution, Refinement and Analysis Program. *J. Appl. Cryst.* **2009**, *42* (2), 339–341.

(67) Sheldrick, G.M. *Acta Cryst.* **2015**, A71, 3-8.

(68) Momma, K.; Izumi, F. VESTA: A Three-Dimensional Visualization System for Electronic and Structural Analysis. *J. Appl. Cryst.* **2008**, *41* (3), 653–658.

(69) Putz, H.; Brandenburg GbR, K. DIAMOND, Bonn, Germany, **2019**.

(70) Frisch, M. J.; Trucks, G. W.; Schlegel, H. B.; Scuseria, G. E.; Robb, M. A.; Cheeseman, J. R.; Scalmani, G.; Barone, V.; Petersson, G. A.; Nakatsuji, H.; Li, X.; Caricato, M.; Marenich, A. V.; Bloino, J.; Janesko, B. G.; Gomperts, R.; Mennucci, B.; Hratchian, H. P.; Ortiz, J. V.; Izmaylov, A. F.; Sonnenberg, J. L.; Williams-Young, D.; Ding, F.; Lipparini, F.; Egidi, F.; Goings, J.; Peng, B.; Petrone, A.; Henderson, T.; Ranasinghe, D.; Zakrzewski, V. G.; Gao, J.; Rega, N.; Zheng, G.; Liang, W.; Hada, M.; Ehara, M.; Toyota, K.; Fukuda, R.; Hasegawa, J.; Ishida, M.; Nakajima, T.; Honda, Y.; Kitao, O.; Nakai, H.; Vreven, T.; Throssell, K.; Montgomery, Jr., J. A.; Peralta, J. E.; Ogliaro, F.; Bearpark, M. J.; Heyd, J. J.; Brothers, E. N.; Kudin, K. N.; Staroverov, V. N.; Keith, T. A.; Kobayashi, R.; Normand, J.; Raghavachari, K.; Rendell, A. P.; Burant, J. C.; Iyengar, S. S.; Tomasi, J.; Cossi, M.; Millam, J. M.; Klene, M.; Adamo, C.; Cammi, R.; Ochterski, J. W.; Martin, R. L.; Morokuma, K.; Farkas, O.; Foresman, J. B.; Fox, D. J. *Gaussian 16, Revision C.01*, Gaussian, Inc., Wallingford CT, 2016.

(71) Becke, A. D. *J. Chem. Phys.* **1993**, *98*, 5648−5652.

(72) Hay P. J.; Wadt, W. R. *J. Chem. Phys.* **1985**, *82*, 299−310.

(73) Roy, L. E.; Hay P. J.; Martin, R. L. *J. Chem. Theory Comput.* **2008**, *4*, 1029−1031.

(74) Ehlers, A. W.; Böhme, M.; Dapprich, S.; Gobbi, A.; Höllwarth, A.; Jonas, V.; Köhler, K. F.; Stegmann, R.; Veldkamp A.; Frenking, G. *Chem. Phys. Lett.* **1993**, *208*, 111−114.

(75) Hariharan P. C.; Pople, J. A. *Theoret. Chimica Acta* **1973**, *28*, 213−222.

(76) Francl, M. M.; Petro, W. J.; Hehre, W. J.; Binkley, J. S.; Gordon, M. S.; DeFrees D. J.; Pople, J. A. *J. Chem. Phys.* **1982**, *77*, 3654−3665.

(77) Clark, T.; Chandrasekhar J.; Schleyer, P. V. R. *J. Comp. Chem.* **1983**, *4*, 294−301.

(78) Krishnam, R.; Binkley, J. S.; Seeger R.; Pople, J. A. *J. Chem. Phys.* **1980**, *72*, 650−654.

(79) Gill, P. M. W.; Johnson, B. G.; Pople J. A.; Frisch, M. J. *Chem. Phys. Lett.* **1992**, *197*, 499−505.

(80) M. J. Frisch, G. W. Trucks, H. B. Schlegel, G. E. Scuseria, W. A. Robb, J. R. Cheeseman, G. Scalmani, V. Barone, B. Mennucci, G. A. Petersson, H. Nakatsuji, M. Caricato, X. Li, H. P. Hratchian, A. F. Izmaylov, J. Bloino, G. Zheng, J. L. Sonnenberg, M. Hada, M. Ehara, K. Toyota, R. Fukuda, J. Hasegawa, M. Ishida, T. Nakajima, Y. Honda, O. Kitao, H. Nakai, T. Vreven, J. A. Montgomery, J. E. Peralta. Jr., F. Ogliaro, M. Bearpark, J. J. Heyd, E. Brothers, K. N. Kudin, V. N. Staroverov, R. Kobayashi, J. Normand, K. Raghavachari, A. Rendell, J. C. Burant, S. S. Iyengar, J. Tomasi, M. Cossi, N. Rega, J. M. Millam, M. Klene, J. E. Knox, J. B. Cross, V. Bakken, C. Adamo, J. Jaramillo, R. Gomperts, R. E. Stratmann, O. Yazyev, A. J. Austin, R. Cammi, C. Pomelli, J. W. Ochterski, R. L. Martin, K. Morokuma, V. G. Zakrzewski, G. A. Voth, P. Salvador, J. J. Dannenberg, S. Dapprich, A. D. Daniels, Ö. Farkas, J. B. Foresman, J. V. Ortiz, J. Cioslowski, D. J. Fox, *Gaussian 09*, *Revision D.01*, Gaussian, Inc., Wallingford CT (2009).

Supplementary Files

This is a list of supplementary files associated with this preprint. Click to download.

- PCCTmagnettransitionSIhm260713.pdf